Journal Pre-proof

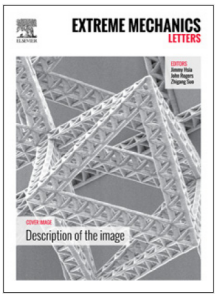

Exploring the inner workings of the clove hitch knot

Tomohiko G. Sano, Paul Johanns, Paul Grandgeorge, Changyeob Baek, Pedro M. Reis

PII: S2352-4316(22)00108-0
DOI: https://doi.org/10.1016/j.eml.2022.101788
Reference: EML 101788

To appear in: *Extreme Mechanics Letters*

Received date : 17 February 2022
Revised date : 11 May 2022
Accepted date : 12 May 2022

Please cite this article as: T.G. Sano, P. Johanns, P. Grandgeorge et al., Exploring the inner workings of the clove hitch knot, *Extreme Mechanics Letters* (2022), doi: https://doi.org/10.1016/j.eml.2022.101788.

Exploring the Inner Workings of the Clove Hitch Knot

Tomohiko G. Sano[**a], Paul Johanns[a], Paul Grandgeorge[†a], Changyeob Baek[‡a,b], Pedro M. Reis[*a]

[a]Flexible Structures Laboratory, Institute of Mechanical Engineering, École Polytechnique Fédérale de Lausanne (EPFL), Lausanne, Switzerland
[b]Department of Mechanical Engineering, Massachusetts Institute of Technology, Cambridge, MA, USA

Abstract

We perform a combined experimental and computational investigation of the clove hitch knot. We develop a physical model for the clove hitch by tying an elastic rod onto a rigid cylinder. In the experiments, we characterize the mechanical performance, geometry, and stability conditions of the knot. X-ray tomography allows us to characterize the 3D geometry of the rod centerline. These results also serve to validate our finite element modeling (FEM), which we use to quantify the tension profile, not accessible experimentally, along the knotted rod. We find that the clove hitch comprises alternating segments with two types of contact regions: one where the rod is in single frictional contact with the cylinder, and another with rod self-contact (where a rod segment pinches another against the cylinder). In the first region, the internal tension decays exponentially (akin to the capstan configuration), whereas, in the second, the pinch (nip) regions lead to discontinuous tension drops. We analyze these nip regions with an even simpler model system where an elastic rod is pinched between two rigid cylinders. Despite the complex contact geometry of this pinching experiment, we find that the frictional behavior of our model systems still obeys the classic Amontons-Coulomb law. Ultimately, we can regard the clove hitch knot, if tied correctly, as a functional structure enabling to drop high tension at one extremity of a filament secured onto a rigid post, all the way to zero at the other extremity.

Keywords:
Physical knots, Friction, Mechanical testing, X-ray tomography, Finite element modeling

1. Introduction

Knotted slender filaments are observed across scales [1], from polymer chains [2, 3] to shipping ropes [1, 4]. Spontaneous knotting is often viewed as a nuisance; *e.g.*, when altering the replication of DNA strands [5–7] or hindering hair combing [8]. By contrast, knots are also used as functional structures in shoelaces [9], surgery [10–12], and climbing [4]. Despite the empirical knowledge amassed over centuries, modeling physical knots is fundamentally challenging due to the nontrivial interplay between topology, geometry, 3D elasticity, and friction. Whereas knot theory has a long history in mathematics [13–16], mechanics-based studies of physical knots remain scarce, although research activity has been increasing in recent years. For example, the mechanics of overhand knots tied on elastic rods has been investigated in loose configurations [17–19]. For tight knots, past studies have focused on purely geometric descriptions (neglecting elasticity and friction) [20], simplified beam-based models [21], and 3D FEM simulations [22], but with limited power to reproduce experimental data. Describing tight physical knots calls for a more realistic set of ingredients, including elasticity and friction. It is then arduous to tackle such systems due to the lack of separation of length scales and cross-sectional deformation, with the additional complication of contact friction. We have recently studied some of the simplest configurations relevant to physical knots, including the orthogonal clasp [23] and the trefoil knot [24, 25]. Nevertheless, modeling the mechanics of more complex knots remains an open problem [26].

The *clove hitch* (see Fig. 1a) is a particularly interesting knot for its wide uses in securing flexible filaments to a rigid post [4], with the remarkable property that it is mechanically stable when there is a sufficiently large tension difference between its two ends. This tension-loss makes it possible to hang a heavy load from a rigid post [4]. The classic capstan equation [27, 28] describes the tension loss for an ideal filament (inextensible, infinitesimally thin, and zero bending stiffness) wrapped, *albeit unknotted*, around a rigid cylinder. Denoting the end tensions as $T_{\text{high}} > T_{\text{low}}$, the capstan equation predicts sliding of the filament when $T_{\text{high}}/T_{\text{low}} > \exp(\mu\theta)$ (θ is the wrapping/contact angle, and μ is the friction coefficient). The capstan problem has been generalized to consider elasticity and finite thickness effects [29–31]. More recently, Grandgeorge *et al.* [32] have proposed a comprehensive framework for this problem, in excellent agreement with experiments. Yet, these models have not been extended to knotted rods, as in the clove hitch. The stability of hitch knots was discussed mathematically, focusing on topological arguments [13], which were later extended for an ideal rope (zero bending stiffness) in frictional contact [14], but the predictions have not yet been validated experimentally.

Here, we explore the mechanics of physical clove hitch knots through a model system comprising an elastic rod tied onto a

*Corresponding author. E-mail address: pedro.reis@epfl.ch (P. M. Reis).
**Current Affiliation: Keio University, Yokohama, Kanagawa, Japan.
†Current Affiliation: University of Washington, Seattle, WA, USA.
‡Current Affiliation: Harvard University, Boston, MA, USA.

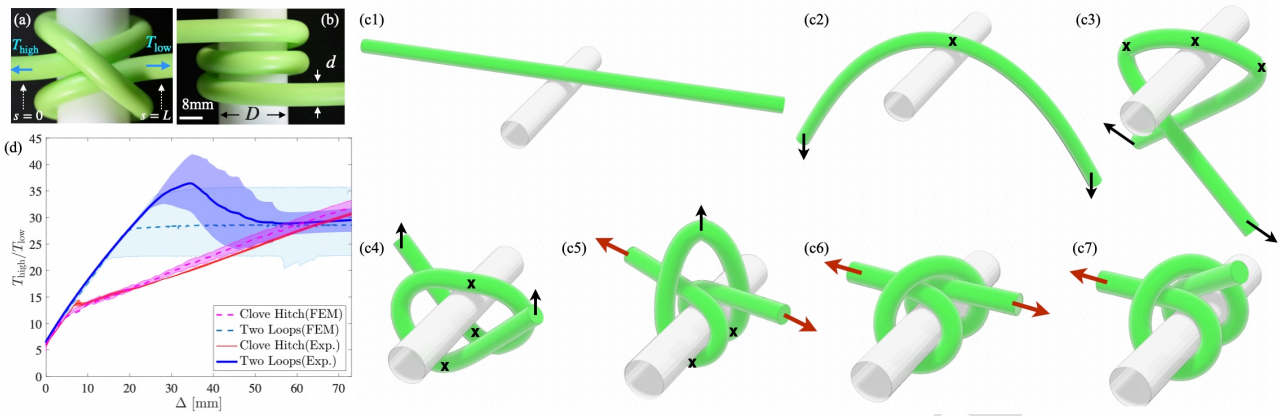

Figure 1: Mechanical performance of the clove hitch knot. Photograph of (a) a clove hitch knot and (b) two loops coiled around a post, with $d = 8\,\text{mm}$ and $D = 25\,\text{mm}$. (c) Protocol to tie the clove hitch in FEM. Nodes marked with **x** are fixed, whereas black and red arrows correspond to displaced and loaded nodes, respectively. The detailed descriptions of the 7 steps are given in Sec. 4. (d) Force-displacement curves for the configurations, with $d = 4\,\text{mm}$ and $D = 30\,\text{mm}$. The solid lines correspond to the experiments (shaded regions represent the standard deviation of 5 independent runs) and the dashed lines to FEM simulations (shaded regions represent the uncertainty associated with the friction coefficient measurements $\mu_{rc} = \mu_{rr} = 0.32 \pm 0.02$). The T_{high}/T_{low} curve does not start from (0, 0) due to the pre-tension; with the reference for zero displacement, $\Delta = 0$, set as detailed in Sec. 5.

rigid cylinder. The methodology we employ builds upon our recent developments in Refs. [23–25, 32], which we extend to more complex geometries and loading conditions. Combining experiments and FEM simulations, we characterize the geometry and tension profile $T(s)$ along the centerline of the knotted rod, analyze the contact regions, and quantify the conditions for sliding. X-ray tomography (μCT) is employed to extract the full 3D geometry of the centerline, serving to validate the FEM simulations. We find that the clove hitch contains alternating segments of two types, depending on the nature of contact: (a) regions where the rod is in frictional contact only with the cylinder (where $T(s)$ decays exponentially), and (b) nip regions (with discontinuous drops in tension due to the pinching of a rod segment by another against the cylinder). These regions, combined, can cause the (high) tension at one end of the rod to drop to zero if the knot is tied correctly. We analyze the tension drop in the nip regions through a simplified model system where an elastic rod is pinched between two rigid cylinders. Despite the complex contact geometry, we find that the frictional behavior of our model systems still obeys the Amontons-Coulomb law within the range of parameters explored.

2. Experimental rod-fabrication protocols

We developed two protocols to fabricate the elastic rods used to tie clove hitch knots for: (a) mechanical testing, and (b) the μCT imaging. Their primary difference is that the latter contained axial fibers and a thin outer coating of 16 % less-dense material (but similar mechanical properties) to enable segmentation during the post-processing of the μCT images.

(a) *For mechanical testing*, we cast naturally straight rods with circular cross-section using vinylpolysiloxane (VPS32, Elite Double 32, Zhermack; Young's modulus $E = 1.26\,\text{MPa}$, density $\rho = 1160\,\text{kg/m}^3$), in straight polyurethane tubes (PUTN3.2-10-W, PUTN6-10-W, Misumi; for inner diameters $d = 2, 4\,\text{mm}$, respectively). Upon curing, the VPS32 rod was demolded, let rest for 7 days to reach steady-state mechanical properties, and cut to the desired length ($9 \le L \le 80\,\text{cm}$). Each rod was surface-treated with talcum powder (Milette, Migros). After a waiting period (~24 hours), robust Amontons-Coulomb behavior was attained with a rod-rod kinetic friction coefficient of $\mu_{rr} = 0.32 \pm 0.02$. The knots were tied onto rigid cylinders made of stainless steel (diameters in the range $20 \le D \le 50\,\text{mm}$), whose surface was also treated to ensure consistent rod-cylinder frictional behavior. First, the cylinders were dip-coated by pulling them out axially from a liquid bath of VPS32 (constant speed, 1 mm/s) to deposit a uniform film (thickness ~ 150 μm) of the same material as the rods [23, 33]. Then, talcum powder was also applied to yield a treated surface with rod-cylinder kinetic friction coefficient of $\mu_{rc} = \mu_{rr}$.

(b) *For μCT scanning*, we adapted an existing protocol [23, 25] to fabricate structured rods optimized for tomographic imaging. These structured rods comprised three parts: (i) a bulk core (VPS32, cast in a straight stainless steel pipe of inner diameter $d = 8.3$ mm; PSTS12A-400, Misumi), (ii) two physical fibers and (iii) an outer coating. The fibers and the coating were made of Solaris (Smooth-On), also a silicone rubber, of mass density $\rho_s = 1001\,\text{kg/m}^3$ and Young's modulus $E_s = 0.32\,\text{MPa}$. The relatively small thickness of both the fibers and the coating (respectively, 500 μm diameter and 150 μm thickness) compared to the rod diameter did not affect the mechanical properties of the rod compared to bulk VPS32. The first fiber was embedded on the central axis of the rod, acting as a physical centerline, $\boldsymbol{r}(s)$. The second one was also set axially, halfway between the centerline and the outer edge of the cross-section. Note that in our previous work [23, 25], only a single central fiber was included (to measure $\boldsymbol{r}(s)$), whereas here, using the same fabrication technique, embedding the second (eccentric) fiber enables the reconstruction of the Cosserat frame $(\hat{\boldsymbol{d}}_1, \hat{\boldsymbol{d}}_2, \hat{\boldsymbol{d}}_3)$ (see Sec. 6.1). The outer coating was introduced to visualize the rod-rod and rod-cylinder contact regions, and was also produced by dip-coating [23]. For the experiments involving μCT scanning,

we used a polyacetal rigid cylinder ($D = 25$ mm), whose mass density, $1410\,\mathrm{kg/m^3}$, is slightly larger than both VPS32 and Solaris, thus facilitating segmentation during post-processing. Similarly to the mechanical testing case, the polyacetal cylinder was also coated and surface-treated to ensure the same frictional properties stated above.

3. FEM simulations

Our FEM simulations were conducted using `ABAQUS/STANDARD`, following a dynamic implicit analysis and considering geometrically nonlinear deformation. A naturally straight rod (diameter $d = 8.6$ mm) was meshed with reduced hybrid 3D solid elements (`C3D8RH`). The number of elements in the cross-section ranged between $\sim$ 100 and $\sim$ 400, sufficient to reproduce experimental results [24]. The typical size of the mesh was $\sim$ 0.4-0.8 mm. We also meshed the outer surface of the rigid and stationary cylinder with rigid elements (`R3D4`), with $\sim$ 1.2 mm for the mesh size. The rod material was modeled as an incompressible neo-Hookean solid (using the experimental value of E). The rod-rod and rod-cylinder contacts were modeled using Amontons-Coulomb friction law; frictional contacts was enforced through normal penalty forces, combined with tangential frictional forces, with a prescribed dynamic friction coefficient [23, 24].

4. Tying the knot in the experiments and simulations

The clove hitch knot consists of two successive half-hitches tied as follows: (i) one end of the rod is looped around the cylinder, (ii) passed back over itself to form a cross, (iii) threaded under itself, (iv) and the system is pulled tight. In Fig. 1(a), we show a photograph of a clove hitch knot. For the μCT imaging (Sec. 6.1) additional care had to be given to the tying process to ensure reproducibility of the final geometry. First, the knot was tied *loosely*, with the rod barely contacting the cylinder. The system was then placed in an ultrasonic bath (VWR, USC1200TH) with a water–soap mixture (Palmolive Original, $\simeq$20% in volume), for 3 minutes (at frequency 45 kHz and temperature 25°C). This step destabilized any still-remaining frictional contacts, ensuring that the equilibrium configuration was reached. After removal from the bath, the system was air-dried at room temperature for $\approx$ 12 hours.

In Fig. 1(c), we present the sequence of 7 steps followed to tie the same knot in FEM. (1) We placed the center of mass of the rod above the rigid cylinder (Fig. 1c1). (2) The centerline mid-point was fixed and the two extremities were displaced to form an arch (Fig. 1c2). (3) Three points of the centerline were fixed and the two extremities were moved horizontally to wrap the rod around the cylinder (Fig. 1c3). (4) The rod extremities were displaced upwards, while fixing three node positions, one at the middle and the other two underneath the cylinder (Fig. 1c4). (5) While fixing the three nodes of the previous step, the middle point was displaced upwards, and the two rod extremities were threaded underneath the opened gap, to attain the clove hitch topology (Fig. 1c5). (6) All nodes were released, expect for the two rod extremities, which were loaded by two forces of the same magnitude but opposite directions to yield a symmetric knot (Fig. 1c5). (7) Asymmetric configurations were realized by reducing one of the loading forces (Fig. 1c6). Note that a similar tying protocol has been introduced in the context of robotics [34].

5. Mechanical testing of the clove hitch knot

We proceed by reporting results on the mechanical performance of the knot, using a universal testing machine (Instron 5943) to obtain force-displacement curves. The knot is tied with a VPS32 rod ($d = 4$ mm) on a rigid cylinder (diameter $D = 30$ mm) using the procedure described above. One end of the knot (at $s = L$) is connected to a dead load $T_{\mathrm{low}} = 0.069$ N ($\simeq 7$ g), while the other (at $s = 0$) is attached to the testing machine to measure the tensile load, T_{high}, as a function of the relative displacement, Δ. To ensure reproducibility, the initial configuration of the knot ($\Delta = 0$) was pre-tensioned as follows. The end at $s = L$ was loaded by an extra weight of 50 g, such that the total dead load was $T_{\mathrm{low}} = 0.559$ N ($\simeq 57$ g). The loading-end at $s = 0$ was then displaced until $T_{\mathrm{high}} = T_{\mathrm{low}} = 0.559$ N, at which point the extra weight of 50 g was removed, returning the dead load to $T_{\mathrm{low}} = 0.069$ N ($\simeq 7$ g). Having completed this pre-tensioning, mechanical testing yielded $T_{\mathrm{high}}(\Delta)$ curves. An identical protocol was implemented in the FEM simulations.

In Fig. 1(d), we plot the rescaled force $T_{\mathrm{high}}/T_{\mathrm{low}}$ across the clove hitch knot, as a function of Δ. The loading force increases nearly monotonically, albeit nonlinearly, with increasing Δ. For $\Delta \lesssim 8$ mm, there is progressive stretching of the rod within the knot but with no relative motion between the rod surface and the cylinder (no sliding); the behavior is linear. Beyond $\Delta \approx 8$ mm, there is frictional sliding between the rod and the cylinder as the clove hitch is tightened further. The curve exhibits a small peak at the onset of sliding motion. In this second regime, $T_{\mathrm{high}}/T_{\mathrm{low}}$ continues to increase significantly, even if at a lower rate than that of the initial linear regime. Excellent agreement is found between the experiments and FEM (solid and dashed pink lines, respectively), serving as a first step in validating the numerics.

To highlight the unique mechanical performance of the clove hitch, we also tested a similar, but topologically simpler, *two-loops* configuration; an elastic rod was wrapped twice around the cylinder (without self-crossings). This configuration can be regarded as a capstan [32] with 4π wrapping angle. The experimental $T_{\mathrm{high}}/T_{\mathrm{low}}$ curve for this two-loops configuration (blue solid line in Fig. 1c) exhibit a peak at $\Delta \simeq 30$ mm, below which the rod stretches, without sliding with respect to the cylinder. For $\Delta \gtrsim 30$ mm, frictional sliding does occur as the configuration is tightened further. Note that no peak was observed in FEM (blue dashed line) since only dynamic friction was considered. For this two-loops case, both experimental and FEM curves tend to a force plateau (above $\Delta \gtrsim 30$ mm), as expected from the capstan equation [27, 28]. By contrast, for the clove hitch, the $T_{\mathrm{high}}/T_{\mathrm{low}}$ curve is monotonically increasing (without a plateau in the explored range of Δ) such that the level of tightening can be adjusted with Δ, evidencing the superior mechanical performance of the knotted versus the two-loop config-

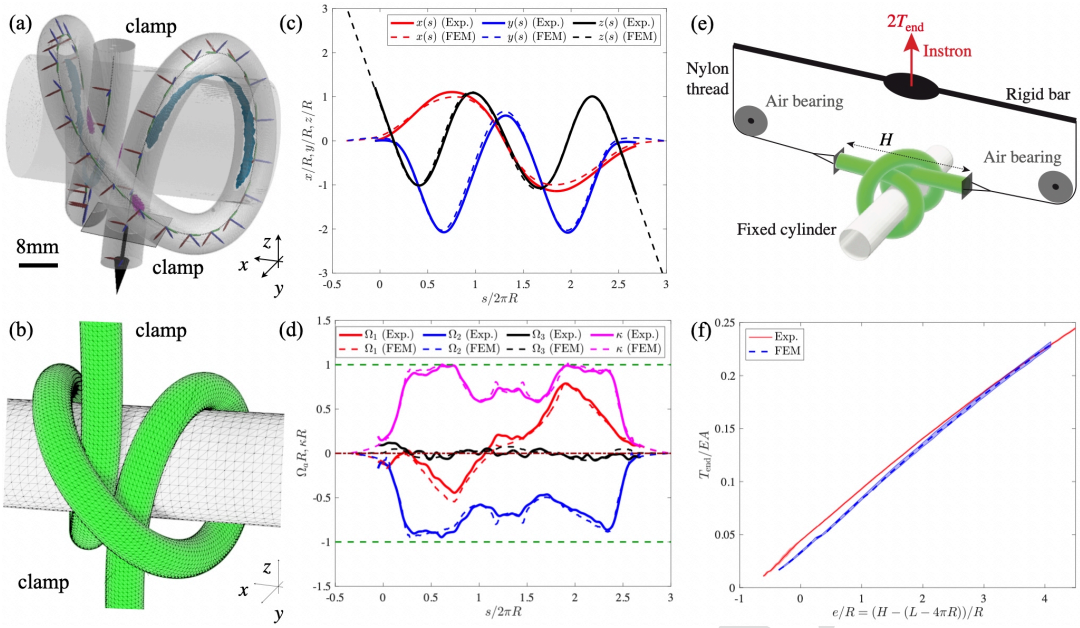

Figure 2: Geometry and mechanics of a symmetric clove hitch knot. (a) Rendering of the μCT-data; $(d,\ D) = (8.6,\ 25)$ mm and $H = 40$ mm for the distance between the two clamped ends. The experimentally measured contact regions are also shown but these data were not processed further. (b) Corresponding FEM-snapshot. (c) Rescaled centerline position $\boldsymbol{r}(s)$ and (d) components of the Darboux vector $\Omega_a(s)$, as functions of the arc length. (e) Schematic of the apparatus used to perform symmetric tensile test of the clove hitch, whose rescaled force-displacement curves (FEM and experiments) are shown in (f).

uration. The superior functionality of the clove hitch originates from the nontrivial coupling between geometry and elasticity. In Sec. 7, we will demonstrate that the self-crossing regions are central to the overall load transmission along the knotted rod.

6. Validation of the FEM: Geometry and Mechanics

Next, we further validate our computational framework against experiments, emphasizing both geometry and mechanics. For simplicity, we turn to a symmetrically-loaded configuration ($T_{\text{high}} = T_{\text{low}}$). In Sec. 6.1, we focus on the 3D geometry of the rod by quantifying the coordinates of the centerline $\boldsymbol{r}(s)$, as well as curvatures and twist. Then, in Sec. 6.2, we complete the FEM validation with mechanical tests for this configuration.

6.1. Geometry of the knot extracted from X-ray tomography

To enable μCT scanning, an VPS32 rod ($d = 8.6$ mm and $L = 350$ mm) was fabricated using protocol (b) described in Sec. 2. A clove hitch knot was then tied onto a polyacetal cylinder following the procedure presented in Sec. 4. The cylinder axis was placed on the $z = 0$ plane and the two ends were clamped at $\boldsymbol{r}(0) = (0,\ 0,\ 20)$ mm and $\boldsymbol{r}(L) = (0,\ 0,\ -20)$ mm. The clove hitch samples were scanned using the X-ray tomograph (μCT 100, Scanco). The 3D images were reconstructed using a built-in software package provided by Scanco, together with a post-processed algorithm developed in-house [23].

In Fig. 2(a), we present a representative example of an experimental μCT reconstruction, with the corresponding FEM-computed configuration in Fig. 2(b). In Fig. 2(c), we characterize the 3D geometry of the knot, plotting the coordinates of the (deformed) centerline, $\boldsymbol{r}(s) = (x(s), y(s), z(s))$, along the normalized arc length $s/(2\pi R)$, where $R \equiv (d + D)/2$ is the effective radius. We find excellent quantitative agreement between experiments and FEM (solid and dashed lines, respectively).

Both in experiments and FEM, we also measured the Darboux vector, $\boldsymbol{\Omega}$, which represents the curvature and twist, as defined next. Let $\hat{\boldsymbol{d}}_3$ be the tangent vector of the centerline, $\hat{\boldsymbol{d}}_3(s) = \boldsymbol{r}'(s)$, where $(\cdot)' \equiv \mathrm{d}(\cdot)/\mathrm{d}s$. At each value of s, two orthonormal vectors $(\hat{\boldsymbol{d}}_1,\ \hat{\boldsymbol{d}}_2)$, are adapted onto the cross-section (normal to $\hat{\boldsymbol{d}}_3$). The triad $\hat{\boldsymbol{d}}_a$ $(a = 1, 2, 3)$, also called *directors*, is known as the Cosserat frame [35]. The basis of the Cosserat frame $\hat{\boldsymbol{d}}_a$ evolves (rotates) along s as

$$\hat{\boldsymbol{d}}_a' = \boldsymbol{\Omega} \times \hat{\boldsymbol{d}}_a \quad (a = 1, 2, 3), \tag{1}$$

where $\boldsymbol{\Omega}$ is the Darboux vector, whose components, $\Omega_a = \boldsymbol{\Omega}\cdot\hat{\boldsymbol{d}}_a$, represent the rotation-rates of the Cosserat frame along s, with respect to $\hat{\boldsymbol{d}}_a$. After measuring the profiles $\hat{\boldsymbol{d}}_a(s)$, the components of the Darboux vector are computed by arranging Eq. (1):

$$\Omega_a = \varepsilon_{abc}\hat{\boldsymbol{d}}_b' \cdot \hat{\boldsymbol{d}}_c, \tag{2}$$

where ε_{abc} is Eddington's epsilon.

Thus, to compute $\Omega_a(s)$, we first need $\hat{\boldsymbol{d}}_a(s)$, reconstructed as follows. From the μCT data, we compute the centerline-tangent, $\hat{\boldsymbol{d}}_3$ from the differentiation of $\boldsymbol{r}(s)$, as $\hat{\boldsymbol{d}}_3 \simeq \{\boldsymbol{r}(s + \mathrm{d}s) - \boldsymbol{r}(s)\}/\mathrm{d}s$. Then, we chose $\hat{\boldsymbol{d}}_1(s)$ to point from the centerline to the eccentric Solaris fiber (see Sec. 2) and compute $\hat{\boldsymbol{d}}_2 \equiv \hat{\boldsymbol{d}}_3 \times \hat{\boldsymbol{d}}_1$, ensuring that the $(\hat{\boldsymbol{d}}_1, \hat{\boldsymbol{d}}_2, \hat{\boldsymbol{d}}_3)$ basis is orthonormal. We iterate this procedure from $s = 0$ to $s = L$, in increments of $\mathrm{d}s = 0.16$mm, using an in-house algorithm developed previously [23, 25]. The FEM-computed Cosserat frame was ob-

tained similarly, with ds set by the mesh size. Finally, with the $\hat{\boldsymbol{d}}_a(s)$ data at hand, from both experiments and FEM, the components of the Darboux vector, $\Omega_a(s)$, could be readily computed using Eq. (2).

In Fig. 2(d), we compare the μCT (solid lines) and FEM (dashed lines) data for the normalized profile of the Darboux vector and the total curvature, $\kappa \equiv (\Omega_1^2 + \Omega_2^2)^{1/2}$. The fidelity of the FEM to quantitatively predict the experimental data is remarkable, despite the complexity of the $\Omega_a(s)$ profiles. The data in Fig. 2(d) highlights the following properties of $\Omega_a(s)$. First, the twist, Ω_3, is significantly smaller than the other two components, Ω_1 and Ω_2. This finding may inform future reduced-order models (beyond the scope of the present study) of the clove hitch knot by assuming $\Omega_3/\kappa \ll 1$. Second, in the regions rod-cylinder contact, the total curvature κ is nearly $1/R$ ($\kappa R \sim 1$, dashed green line in Fig. 2d), meaning that the rod wraps the cylinder with its tangent normal to the cylinder axis. Third, Ω_2 remains negative all along s, whereas Ω_1 changes sign half-way, further conveying the complexity of the geometry.

6.2. *Mechanical test of the symmetric clove hitch knot*

The detailed characterization in the previous section established an important step in the FEM validation, but was purely geometrical. Next, we further attest the capability of the FEM to predict the mechanics of the clove hitch under symmetric loading, using the experimental apparatus shown in Fig. 2(e). The rigid cylinder was fixed and the two ends of the rod were loaded by the mechanical testing machine via two nylon filaments (StroftN, Waku GmbH), realigned by two air bearings (IBS Precision Engineering), and attached to a rigid bar. This bar was displaced upwards (imposed end-to-end distance H), while measuring the end force $2T_{\text{end}}$ (T_{end} on each extremity). In Fig. 2(f), we plot the rescaled force-displacement curve, with $T_{\text{end}}/(EA)$ as a function of the end-to-end extension $e \equiv H-(L-4\pi R)$ [17] with the cross-sectional area $A = \pi d^2/4$. Note that $e = 0$ corresponds to the case of the centerline wrapping twice around the cylinder. We find that the end-force increases monotonically with e, mostly dominated by the stretching of the material, and the experiments are, again, in excellent agreement with FEM.

7. Tension-loss in the clove hitch knot

The predictive power of the FEM to reproduce the experimental results demonstrated above gives us confidence to now rely purely on FEM to access a quantity and conditions not accessible experimentally. Specifically, we explore the internal tension profile along the rod, $T(s)$, and the effect of the rod-cylinder friction coefficient. The latter is challenging to vary systematically in the experiments without introducing additional artifacts.

Going beyond the symmetric configuration considered above, we now consider the more practically relevant asymmetric case, with a free extremity ($T_{\text{low}} = 0$). The simulations were performed using the following set of parameters: fixed geometry (d, D, L) = (4, 30, 374) mm, rod-rod friction coefficient

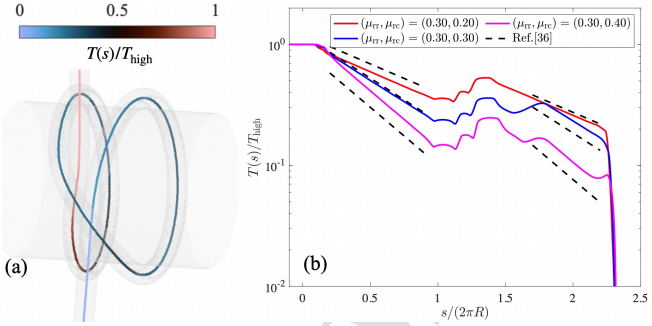

Figure 3: Characterization of the tension $T(s)$ along the clamped-free clove hitch knot obtained from FEM. Rescaled tension profile $T(s)/T_{\text{high}}$ (a) superposed on the 3D configuration and (b) plotted (solid lines) versus $s/(2\pi R)$. Three curves are provided for different values of μ_{rc}, while fixing μ_{rr} (see legend). The dashed lines are exponential decays based on Ref. [36]. The data points are the value of the tension at $s/(2\pi R) = 2.25$, near the free-end.

$\mu_{\text{rr}} = 0.3$, loading condition $T_{\text{high}} = 1.47$ N, and three values of the rod-cylinder friction coefficient $\mu_{\text{rc}} = \{0.2, 0.3, 0.4\}$. The internal tension $T(s) \equiv -\boldsymbol{F}(s) \cdot \hat{\boldsymbol{d}}_3(s)$ is computed from the resultant internal force $\boldsymbol{F}(s) = \boldsymbol{F}(L) + \int_s^L \boldsymbol{p}(s')\mathrm{d}s'$ acting on the cross-section at s, exerted by portion of the rod with $\tilde{s} > s$ on the portion with $\tilde{s} < s$, accounting for the contact forces per unit-length $\boldsymbol{p}(s)$ [32]. A representative example (for $\mu_{\text{rc}} = 0.3$) is shown in Fig. 3(a), where we plot value of $T(s)/T_{\text{high}}$ on the 3D reconstruction of the rod centerline. We find that the high-tension at one end decays to zero past the knot.

In Fig. 3(b), we compare $T(s)$ for the three cases with different values of μ_{rc}, while fixing μ_{rr}. The three curves exhibit two important features: (i) $T(s)$ decays exponentially in the regions of rod-cylinder contact (cf. dashed lines in Fig. 3b); and (ii) $T(s)$ is non-exponential in the regions with (rod-rod) self-contact. There are three non-exponential regions, two of which are drops in $T(s)$ found at the entrance, $s/(2\pi R) \approx 0.1$, and exit, $s/(2\pi R) \approx 2.25$, of the knot. In the third non-exponential region, in the middle of the knot, $1.0 < s/(2\pi R) < 1.5$, the tension increases because the direction of the contact frictional forces is opposite to that of the other regions where $T(s)$ decreases. The decay rate of the exponential depends on μ_{rc}, as expected from the classical Capstan problem [27, 28]. Indeed, the capstan problem with a finite-thickness rod [36] predicts that, away from the loading-ends,

$$T(s) \sim \exp\left(-\mu_{\text{eff}} \frac{s}{R}\right), \tag{3}$$

where $\mu_{\text{eff}} \equiv \{-(1+\tilde{D}) + \sqrt{(1+\tilde{D})^2 + 4\mu_{\text{rc}}^2 \tilde{D}}\}/(2\mu_{\text{rc}})$ is the effective friction coefficient and $\tilde{D} = D/d$. The predictions from Eq. (3) are plotted in Fig. 3(b) as dashed lines, whose slopes are in excellent agreement with FEM. Hence, the tension decay of the clove hitch along the rod-cylinder contact regions can be interpreted under the framework of the capstan problem.

Predicting $T(s)$ in the rod-rod contact (nip) regions involves, at least, the following two theoretical challenges. First, the contact problem is non-local; the internal force, $\boldsymbol{F}(s)$, is computed once the contact force density $\boldsymbol{p}(s')$ for $s \le s' \le L$ is known. Yet, the force density at the rod-rod contact $\boldsymbol{p}(s)$ is affected by

the remaining contact regions in $0 \le s'' \le s$ (via the law of action-reaction). Second, the nip regions involve large cross-sectional deformation. Therefore, centerline-based (Kirchhoff) theories [35] become inappropriate [23, 32], requiring material nonlinearities to be taken into account.

Whereas addressing the above theoretical challenges is beyond the scope of the present study, we have performed two additional sets of experiments to gain further physical insight into these issues, which are addressed next, in Sec. 8 and Sec. 9.

8. Stability of the clove hitch knot

The issue of non-locality of the contact has been partially incorporated in past literature [14], predicting that, when the hitch knot slips, the larger load of the two extremities, T_{high}, is linear to the other load T_{low}. Thus, when $T_{\text{low}} = 0$, the clove hitch knot is expected to slip at $T_{\text{high}} = 0$. In other words, the clove hitch slips independently of the rod or cylinder diameters. To test this prediction, we have experimentally characterized the stability of the clove hitch with a free end ($T_{\text{low}} = 0$). First, we tied the clove hitch knot loosely onto the cylinder. Then, we attached a calibrated weight T_{high} to the other extremity at $s = 0$ and observed whether the knot was stable or became undone (failure). Each run was repeated five times under the same conditions to test reproducibility. The knot was deemed *stable* if slippage did not occur in any of the five runs. *Failure* was reported if the knot became undone at least once.

In Fig. 4, we plot the stability diagram for these experiments, normalizing T_{high} by the axial stiffness EA. The phase boundary between stable and failure behavior (the critical load for slippage) depends on the rescaled diameter $d/2R$. These results are decidedly not in agreement with the predictions from Ref. [14] (vertical dashed line in Fig. 4), thereby calling for more detailed theoretical analysis to model the clove hitch knot.

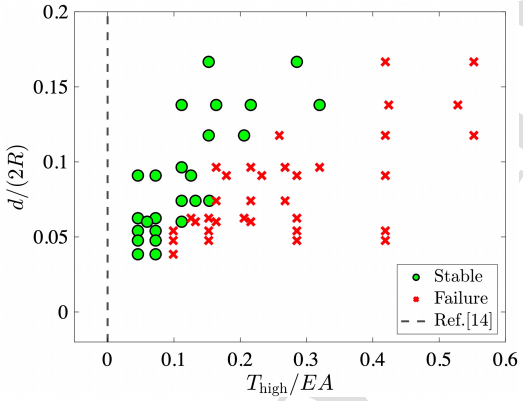

Figure 4: Experimental stability phase diagram of the clove hitch knot. The dashed line is predicted from Ref. [14].

9. Pinching of an elastic rod

Finally, we study the nip regions and attempt to gain insight on how the cross-sectional deformation may affect the rod-sliding behavior. We considered a further-simplified configuration where a short VPS32 rod segment (length 9 cm) was sandwiched (pinched) between two VPS-coated rigid cylinders (diameter $D = 8$ mm). The axis of the rod was set perpendicularly to the axes of the rigid cylinders. The experimental apparatus is shown in Fig. 5(a, b). The lower cylinder was fixed. The upper cylinder was connected to a counter weight, through a linear air bearing (IBS Precision Engineering), an inextensible filament, and two pulleys. As such, the upper cylinder applies a known normal load, F_n, onto the rod. The rod was connected, through a filament/pulley system, to the mechanical testing machine measuring the tangential force, F_t^*, required to overcome the frictional forces (slippage onset). This setup was designed to mimic the contact geometry near the free-end of the clove hitch, where the tension $T(s)$ drops to zero (see open triangles in Fig. 3b).

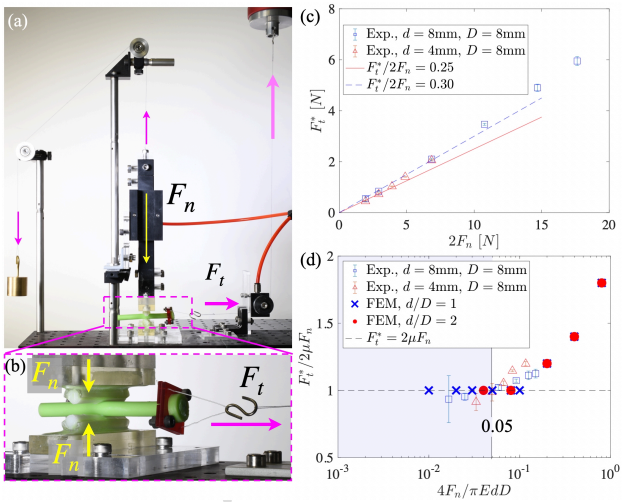

Figure 5: Friction measurement of pinched elastic rod. (a) Experimental setup. The elastic rod is pinched by two rigid cylinders. One cylinder is attached with the vertical air bearing to a counter weight. (b) Zoomed view of the pinched elastic rod. (c) The experimental data on the friction force F_t^* as a function of the normal load $2F_n$. The dashed and solid lines fit the smaller load F_n; the slope represents their effective friction coefficient μ. (d) The rescaled friction force $F_t^*/(2\mu F_n)$ versus the rescaled normal load $F_n/(\pi EdD/4)$. The shaded regions represent $4F_n/\pi EdD \le 0.05$ (see Sec. 9).

In Fig. 5(c), we plot F_t^* *vs.* F_n, for two VPS32 rods ($d = \{4, 8\}$ mm). At low values of F_n, the critical tangential force for sliding is described well by Amontons-Coulomb's law $F_t^* = 2\mu F_n$ (both contact surfaces contribute to the sliding, hence, the factor of 2), as conveyed by the linear fit. However, this behavior changes for larger values of F_n. To better examine how F_t^* deviates from Amontons-Coulomb's behavior, in Fig. 5(d), we plot the ratio $F_t^*/(2\mu F_n)$ as a function of the rescaled normal load $4F_n/(\pi EdD)$. Results from the equivalent FEM simulations are also included in the plot. Whereas Amontons-Coulomb law holds for $4F_n/(\pi EdD) \lesssim 0.1$, we find significant deviations beyond this point, presumably due to geometrically nonlinear deformation of the pinched cross-section.

It is interesting to note that this violation of the Amontons-Coulomb's behavior does not seem to play a significant role in the stability experiment (Sec. 8). Indeed, from Fig. 4, we

found that the upper bound of the critical sliding force is expected at $T_{\text{high}}/EA \approx 0.3$, for the range of parameters considered. Also, from the tension profiles in Fig. 3(b), the dead load T_{high} exerted at $s = 0$ decays toward nearly $\approx 18\%$ between the clamped end and the last nip-region near the free end. Hence, translating this value into the dimensionless force yields $4F_n/(\pi EdD) \approx 0.05$ (vertical solid line in Fig. 5d), which still lies within the regime where Amontons-Coulomb law is valid (shaded region in Fig. 5c). This estimation suggests that, for future theoretical analysis of the clove hitch, and potentially for other knots, it may be sufficient to consider Amontons-Coulomb to model frictional interactions.

10. Conclusion

Combining precision experiments and FEM simulations, we studied the mechanics of the clove hitch knot, regarding it as a functional structure capable of transforming high tension in a rod down to zero. As such, these knots are particularly useful to tie a weight from a rigid cylinder. The topology of the clove hitch, and the nip regions with rod-rod contact, are central to their mechanical behavior, as demonstrated by contrast to the two-loops (capstan-like) configuration.

We characterized the complex 3D geometry of the clove hitch knot using μCT, experimentally measuring the centerline position and the Darboux vector components, in excellent agreement with FEM. To the best of our knowledge, these data are the first of their kind in the rod mechanics community. We then relied on FEM to quantify the tension profile, which is not readily accessible experimentally, uncovering the two qualitatively different regions. First, we saw a capstan-like exponential decay of the tension, consistently with literature [36]. Secondly, the nip regions were found to be responsible for (non-exponential) tension drops, underlying the unique mechanical performance of this knot. We also characterized the stability of the clove hitch, finding that the failure onset deviates from existing simplified models. Investigation of a simpler model system suggested that Amontons-Coulomb's frictional behavior is appropriate, at least in the range of parameters explored.

Although the clove hitch is one of the simplest, albeit among the most useful, functional knots, the coupling between elasticity, friction, and nonlinear geometry leads to extremely rich mechanics. We hope that our results will help to continuing opening the door for future theoretical models that go beyond the relatively simple configurations studied to date.

Acknowledgments. This work was supported by the Fonds National de la Recherche, Luxembourg (12439430), the Grants-in-Aid for JSPS Overseas Research Fellowship (2019-60059), and by MEXT KAKENHI 18K13519.

References

[1] J. C. Turner, P. van De Griend (Eds.), History and Science of Knots, World Scientific, Singapore, 1996.
[2] P. G. de Gennes, Dynamics of entangled polymer solutions. I. the rouse model, Macromolecules 9 (1976). doi:10.1021/ma60052a011.
[3] L. Tubiana, A. Rosa, F. Fragiacomo, C. Micheletti, Spontaneous knotting and unknotting of flexible linear polymers: Equilibrium and kinetic aspects, Macromolecules 46 (2013) 3669–3678. doi:10.1021/ma4002963.
[4] C. W. Ashley, The Ashley Book of Knots, New York: Doubleday, 1944.
[5] A. D. Bates, A. Maxwell, O. Press, DNA Topology, Oxford University Press, New York, 2005.
[6] Y. Arai, R. Yasuda, K.-I. Akashi, Y. Harada, H. Miyata, K. Kinosita, H. Itoh, Tying a molecular knot with optical tweezers, Nature (1999) 399, 446–448.
[7] J. Arsuaga, M. Vazquez, S. Trigueros, D. W. Sumners, J. Roca, Knotting probability of DNA molecules confined in restricted volumes: DNA knotting in phage capsids, Proceedings of the National Academy of Sciences 99 (2002) 5373–5377. doi:10.1073/pnas.032095099.
[8] J. Hughes, T. Plumb-Reyes, N. Charles, L. Mahadevan, D. Rus, Detangling hair using feedback-driven robotic brushing, in: 2021 IEEE 4th International Conference on Soft Robotics (RoboSoft), IEEE, 2021. doi:10.1109/robosoft51838.2021.9479221.
[9] C. A. Daily-Diamond, C. E. Gregg, O. M. O'Reilly, The roles of impact and inertia in the failure of a shoelace knot, Proc. Math. Phys. Eng. Sci. 473 (2017) 20160770. doi:10.1098/rspa.2016.0770.
[10] R. F. Edlich, in: A. G. Covidien (Ed.), Surgical Knot Tying Manual, Third Edition, 150 Glover Avenue Norwalk, CT 06856, 2008.
[11] F. W. Taylor, Surgical knots, in: Ann Surg., volume 107(3), 1938, pp. 458–68.
[12] P. Calhoun, Advanced surgical knot tying, Independently Published 2nd Edition (2016).
[13] B. F. Bayman, Theory of hitches, American Journal of Physics (1977) 185–190. doi:10.1119/1.10652.
[14] J. H. Maddocks, J. B. Keller, Ropes in equilibrium, SIAM J. Appl. Math. 47 (1987) 1185–1200. doi:10.1137/0147080.
[15] H. Gerlach, Ideal Knots and Other Packing Problems of Tubes, Ph.D. thesis, EPFL, 2010. doi:10.5075/epfl-thesis-4601, Additional data: URL: https://lcvmwww.epfl.ch/publications/data/phd/10/data/.
[16] T. Deguchi, E. Uehara, Statistical and dynamical properties of topological polymers with graphs and ring polymers with knots, Polymers 9 (2017). doi:10.3390/polym9070252.
[17] B. Audoly, N. Clauvelin, S. Neukirch, Elastic knots, Phys. Rev. Lett. 99 (2007). doi:10.1103/physrevlett.99.164301.
[18] N. Clauvelin, B. Audoly, S. Neukirch, Matched asymptotic expansions for twisted elastic knots: a self-contact problem with nontrivial contact topology, J. Mech. Phys. Solids 57 (2009) 1623–1656. doi:10.1016/j.jmps.2009.05.004.
[19] M. Jawed, P. Dieleman, B. Audoly, P. Reis, Untangling the mechanics and topology in the frictional response of long overhand elastic knots, Phys. Rev. Lett. 115 (2015). doi:10.1103/physrevlett.115.118302.
[20] P. Pierański, S. Kasas, G. Dietler, J. Dubochet, A. Stasiak, Localization of breakage points in knotted strings, New J. Phys. 3 (2001) 10–10. doi:10.1088/1367-2630/3/1/310.
[21] D. Durville, Contact-friction modeling within elastic beam assemblies: an application to knot tightening, Comput Mech 49 (2012) 687–707. doi:10.1007/s00466-012-0683-0.
[22] A. Y. Q. Alden, A. G. Geeslin, J. C. King, P. A. Gustafson, A finite element model of a surgical knot, in: Volume 3: Biomedical and Biotechnology Engineering, ASME, 2017. doi:10.1115/imece2017-72201.
[23] P. Grandgeorge, C. Baek, H. Singh, P. Johanns, T. G. Sano, A. Flynn, J. H. Maddocks, P. M. Reis, Mechanics of two filaments in tight orthogonal contact, Proceedings of the National Academy of Sciences 118 (2021). doi:10.1073/pnas.2021684118.
[24] C. Baek, P. Johanns, T. G. Sano, P. Grandgeorge, P. M. Reis, Technical brief: Finite element modeling of tight elastic knots, Journal of Applied Mechanics (2020) 1–7. doi:10.1115/1.4049023.
[25] P. Johanns, P. Grandgeorge, C. Baek, T. G. Sano, J. H. Maddocks, P. M. Reis, The shapes of physical trefoil knots, Extreme Mechanics Letters 43 (2021). doi:10.1016/j.eml.2021.101172.
[26] V. P. Patil, J. D. Sandt, M. Kolle, J. Dunkel, Topological mechanics of knots and tangles, Science 367 (2020) 71–75. doi:10.1126/science.aaz0135.
[27] L. Euler, Remarques sur l'effet du frottement dans l'equilibre, Memoires de l'academie des sciences de Berlin - (1769) 265–278.
[28] J. A. Eytelwein, Handbuch der Statik fester Körper: mit vorzüglicher Rücksicht auf ihre Anwendung in der Architektur, volume 1, Reimer,

1832.
[29] I. M. Stuart, Capstan equation for strings with rigidity, J. Appl. Phys. 12 (1961) 559–562. doi:10.1088/0508-3443/12/10/309.
[30] J. H. Jung, T. J. Kang, J. R. Youn, Effect of bending rigidity on the capstan equation, Textile research journal 74 (2004) 1085–1096.
[31] J. H. Jung, N. Pan, T. J. Kang, Generalized capstan problem: Bending rigidity, nonlinear friction, and extensibility effect, Tribol Int 41 (2008) 524–534. doi:10.1016/j.triboint.2007.11.005.
[32] P. Grandgeorge, T. G. Sano, P. M. Reis, An elastic rod in frictional contact with a rigid cylinder, Journal of the Mechanics and Physics of Solids 164 (2022) 104885. doi:10.1016/j.jmps.2022.104885.
[33] L. Landau, B. Levich, Dragging of a liquid by a moving plate, in: Dynamics of Curved Fronts, Elsevier, 1988, pp. 141–153. doi:10.1016/b978-0-08-092523-3.50016-2.
[34] L. He, Q. Zhang, X. Du, R. Luo, M. Karkee, A twining robot for high-trellis string tying in hops production, Transactions of the ASABE 55 (2012) 1667–1673. doi:10.13031/2013.42351.
[35] B. Audoly, Y. Pomeau, Elasticity and Geometry, Oxford Univ. Press, 2010.
[36] J. H. Jung, N. Pan, T. J. Kang, Capstan equation including bending rigidity and non-linear frictional behavior, Mech Mach Theory 43 (2008) 661–675. doi:10.1016/j.mechmachtheory.2007.06.002.

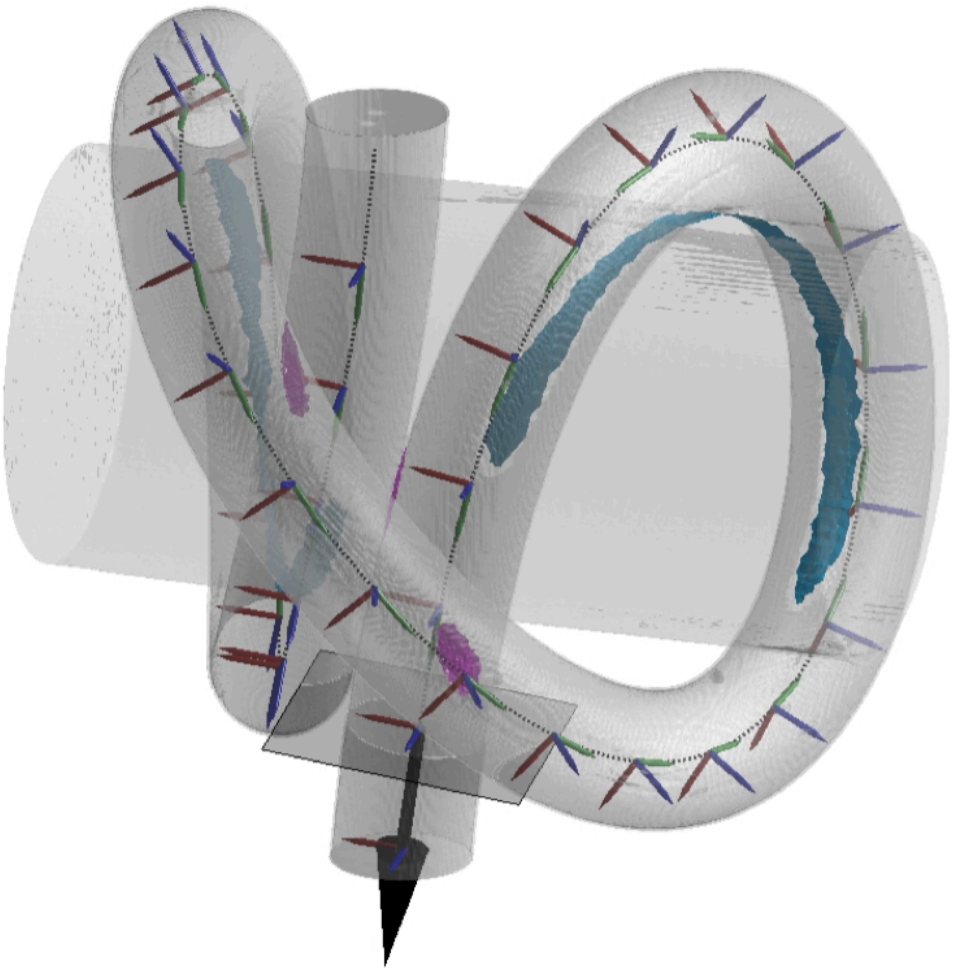

Declaration of Competing Interest: The authors declare that they have no known competing financial interests or personal relationships that could have appeared to influence the work reported in this paper.